

Expedited Noise Spectroscopy of Transmon Qubits

Bhavesh Gupta,^{1,2,*} Vismay Joshi,^{1,2,*} Udit Kandpal,^{1,2} Prabha Mandayam,^{1,2} Nicolas Gheeraert,^{1,3} and Siddharth Dhomkar^{1,2,†}

¹*Department of Physics, Indian Institute of Technology Madras, Chennai - 600036, India*

²*Center for Quantum Information, Communication and Computing, Indian Institute of Technology Madras, Chennai - 600036, India*

³*School of Interwoven Arts and Sciences (SIAS), Division of Sciences, Krea University, Sri City - 517646, India*

(Dated: February 4, 2025)

There has been tremendous progress in the physical realization of quantum computing hardware in recent times, bringing us closer than ever before to realizing the promise of quantum computing. However, noise continues to pose a crucial challenge when it comes to scaling up present day quantum processors. While decoherence limits the qubits' ability to store information for long periods in the presence of uncontrollable noise sources, the erroneous implementation of control methods for state preparation and measurements leads to faulty implementations of quantum circuits. Conventional noise spectroscopy protocols can characterize and model environmental noise but are usually resource intensive and lengthy. Moreover, the underlying noise can vary in nature over time, making noise profile extraction futile as this new information cannot be harnessed to improve quantum error correction or dynamical decoupling protocols. In this work, we address this challenge using a machine learning-based methodology to quickly extract noise spectra of multiple qubits and demonstrate a possible noise mitigation strategy. The procedure involves implementing undemanding dynamical decoupling sequences to record coherence decays of the investigated qubits and then predict the underlying noise spectra with the help of a convolution neural network pre-trained on a synthetic dataset. While our protocol is virtually hardware-agnostic, we validate its effectiveness using superconducting qubits available on the IBM Quantum platform. We further use these rapidly obtained, yet accurate, noise spectra to design bespoke dynamic decoupling sequences and perform time-dependent noise spectroscopy.

I. INTRODUCTION

Decoherence [1–3] refers to the loss of coherence in a quantum system due to unavoidable interactions with its environment. Decoherence remains the Achilles heel in developing practical quantum technologies such as quantum computation [4, 5], and quantum sensing [6, 7]. Understanding and controlling noise leading to decoherence in quantum systems is therefore an important task in the context of building robust and scalable quantum processors. To this end, one needs to understand the nature of this noise, identify its possible sources, and efficiently curb it with the available tools.

Characterizing and modeling noise using conventional spectroscopic methods, requires abundant resources. The way to extract a spectrum of noise that affects a system is based on deconvolution of the spectral overlap of the noise power spectral density function and the corresponding quantum control protocol used to probe the system [8]. This control method can also be a dynamical error suppression protocol, such as dynamical decoupling (DD) [9–16], which is a general method to preserve spin coherence in the presence of noise. The control acts as a filter, allowing one to probe a specific region of the broad frequency spectrum affecting the quantum system. This

can be modeled analytically with the help of the filter function formalism [8, 17]. Conversely, understanding the spectrum of the noise acting on a qubit crucially underpins the optimization of DD protocols that can mitigate such noise. In practice, the noise spectrum varies significantly across different qubits in non-trivial ways that are hard to predict or accurately extract from most common measurements. As a result, it is difficult to predict *a priori* which of the several possible DD protocols would provide optimal suppression of decoherence. Indeed, one could imagine constructing a decoupling protocol customized for a particular qubit, but this is possible only if the knowledge of the actual qubit noise spectrum is available with sufficient accuracy. Furthermore, the design and implementation of efficient quantum error correction (QEC) [18–20] protocols and fault-tolerant quantum circuits [21], often requires an understanding of the specific noise affecting the qubits; rapid extraction of noise spectra thus becomes an imperative tool for both error mitigation and error correction.

Extracting noise spectra rapidly for qubits presents several challenges. Conventional long-duration noise spectroscopy protocols require extended measurement times and repeated implementation [22]. Thus, for time-dependent noise, the measured noise spectrum becomes a distorted representation of the actual noise affecting the qubit. Furthermore, other complex pulse sequences with minimal spectral leakage can allow noise extraction with relatively fewer experimental runs [23]; however, these strategies require unique resources and usually have re-

* Equal contribution to this work.

† sdhomkar@physics.iitm.ac.in

duced sensitivity. Here, we address the challenge of rapid noise spectroscopy with the help of deep learning algorithms. Owing to their success in diverse domains, there has been a thrust to utilize the power of artificial neural networks to characterize and correct the deleterious environmental effects [24–28]. In this study, we extend the neural network-based methodology [24, 25] to rapidly predict the time-varying noise spectral densities associated with the state-of-the-art transmon qubits. Moreover, we propose a proof-of-principle method to mitigate the environmental noise by constructing customized dynamical decoupling sequences.

The rest of the paper is organized as follows. In Sec. II, we discuss the mathematical framework for modeling noise in quantum systems and highlight the importance of accurately discerning the environmental noise. We also recall the link between the extracted noise spectrum and the error rates corresponding to various noise sources [29]. Sec. III details our methodology. Therein, we demonstrate how a deep neural network can be trained to extract the noise spectrum from typical time dynamics measurements such as Hahn echo and Carr-Purcell-Meiboom-Gill (CPMG)-32. We then provide an overview of the experimental data processing and DD optimization procedure. In Sec. IV, we benchmark our model’s effectiveness in extracting and mitigating the noise for the IBM Quantum superconducting quantum architecture. Finally, in Sec. V, we conclude with critical discussion and propose future directions.

II. SIGNIFICANCE OF THE ‘DECOHERENCE FUNCTIONAL’

The Lindblad master equation offers a powerful and elegant way to describe the dynamics of open quantum systems [31]. This formalism translates the complex interplay between system and environment into a set of linear, non-Hermitian operators known as Lindblad operators, which capture the essence of various noise processes such as relaxation and dephasing [32]. If the noise sources are weakly coupled to the qubits and have short correlation times with respect to the system dynamics, the relaxation processes are characterized by two rates [33], namely,

$$\text{Longitudinal relaxation rate: } \Gamma_1 = \Gamma_{1\uparrow} + \Gamma_{1\downarrow} \equiv \frac{1}{T_1}$$

$$\text{Transversal relaxation rate: } \Gamma_2 = \frac{\Gamma_1}{2} + \Gamma_\phi \equiv \frac{1}{T_2},$$

Here, the T_1 time corresponds to the energy relaxation process, while T_ϕ represents pure dephasing and $\Gamma_\phi = 1/T_\phi$ is the pure dephasing rate. The total decoherence time T_2 reflects the loss of coherence caused by both energy relaxation and pure dephasing. The noisy density matrix ρ_{noisy} for the qubit after the impact of noise can then be written as [34],

$$\rho = \begin{pmatrix} |\alpha|^2 & \alpha\beta^* \\ \alpha^*\beta & |\beta|^2 \end{pmatrix} \xrightarrow{\text{noise}} \rho_{\text{noisy}} = \begin{pmatrix} 1 + (|\alpha|^2 - 1)e^{-\Gamma_1 t} & \alpha\beta^* e^{-\Gamma_2 t} \\ \alpha^*\beta e^{-\Gamma_2 t} & |\beta|^2 e^{-\Gamma_1 t} \end{pmatrix} \quad (1)$$

In this weak coupling limit with short correlation times, the phase decay function is simply given by $e^{-\Gamma_2 t}$. Furthermore, it is important to note that the T_1 relaxation noise process is incoherent and non-unitary, thus making it irreversible via purely unitary operations. However, the dephasing noise corresponding to T_ϕ can be mitigated by carefully designing appropriate control pulse sequences.

Table I presents the common noise sources in a transmon architecture, highlighting the types of coupling between the noise and qubit axes that contribute to decoherence across different frequency regimes. In superconducting qubits, the broadband dephasing noise – including, for example, flux noise, charge noise, and critical-current noise – tends to exhibit a $1/f$ -like power spectrum, as mentioned in Table I. Such noise is singular near $\omega = 0$, has long correlation times, and generally *does not fall* within the Bloch-Redfield description [30]. In this case, the decay function of the off-diagonal terms in Eq. (1) is generally non-exponential, and for such cases, the simple expression $\Gamma_2 = \Gamma_1/2 + \Gamma_\phi$ is *not applicable*.

For $1/f$ noise spectra, the phase decay function is itself a Gaussian $\exp[-(t/T_{\phi,G})^2]$ (stretched exponential decay) [30]. Furthermore, this function is separable from the T_1 -type exponential decay because the T_1 -noise remains regular at the qubit frequency. Therefore, the modified density matrix after the action of noise is now given by [30],

$$\rho = \begin{pmatrix} 1 + (|\alpha|^2 - 1)e^{-\Gamma_1 t} & \alpha\beta^* e^{-\frac{\Gamma_1}{2} t} e^{-\chi(t)} \\ \alpha^*\beta e^{-\frac{\Gamma_1}{2} t} e^{-\chi(t)} & |\beta|^2 e^{-\Gamma_1 t} \end{pmatrix}. \quad (2)$$

Here, the decay function $e^{-\chi(t)}$ is characterized by the *decoherence functional* $\chi(t)$, which generalizes pure dephasing to include non-exponential decay functions. Because the function is no longer purely exponential, we cannot formally write the transverse relaxation decay function as e^{-t/T_2} .

The decoherence functional $\chi(t)$ is related to the noise spectrum or power spectral density (PSD) $S(\omega)$ as follows.

$$\chi(t) = -\ln C(t) = \int_0^\infty \frac{d\omega}{\pi} S(\omega) \frac{F(\omega t)}{\omega^2}. \quad (3)$$

Here, $C(t)$ denotes the coherence curve and $F(\omega t)$ is the filter function associated with a given pulse sequence. In addition to $1/f$ -type dephasing mechanisms, there are also “white” pure dephasing mechanisms, which give rise to an exponential decay function for the dephasing component of T_2 . The noise spectrum $S(\omega)$ thus exclusively characterizes the dephasing mechanism.

Sources	Arises from	Type of coupling with qubit	$S(\omega)$
Charge Noise	Charge fluctuators present in the defects or charge traps that reside in interfacial dielectrics, the junction tunnel barrier, and in the substrate itself.	Dominant: Transverse (T_1) Sometimes low frequency (T_ϕ)	At low frequency $\propto 1/\omega$ At high frequency $\propto \omega$
Magnetic Flux Noise	Stochastic flipping of qubits that reside on the surfaces of the superconductors, resulting in random fluctuations of effective- \vec{B} that biases flux-tunable qubits.	Transverse (T_1) Longitudinal (T_ϕ)	$\propto 1/\omega$
Photon Number Fluctuations	In resonator, residual microwave fields in the cavity have photon number fluctuations.	Longitudinal (T_ϕ)	$\propto \frac{k}{\omega^2 + k^2}$ k : resonator decay rate
Quasiparticles	Unpaired electrons tunneling through a qubit junction	Transverse (T_1) Longitudinal (T_ϕ)	$\propto \frac{N_{qp}\tau_{qp}}{\omega^2 + \tau_{qp}^2}$ τ_{qp} : quasiparticle lifetime
Local two level system (TLS)	Electric dipole moment resonantly absorb energy from the oscillating \vec{E} of the qubit mode, and efficiently dissipate it into the phonon or quasiparticle bath.	Transverse (T_1) Longitudinal (T_ϕ)	Low freq.: White noise, $1/\omega$ High freq.: Lorentzian type

TABLE I. Summary of common noise sources in transmon systems [30], their frequency dependencies, and coupling mechanisms with qubits.

It is important to note here that the noisy density matrix in Eq. (1) is equivalent to what one may obtain using the Kraus operator-sum description of noise in quantum systems [34]. The Kraus operators describe the decoherence resulting from the interaction between the system and its environment over a period of time. The form of the Kraus operators takes into account the decoherence functional, as explained in Appendix A. The density matrix in Eq. (1) is thus identical to the density matrix in Eq. (A3) obtained due to the combined effect of the dephasing and amplitude-damping channels on the initial density matrix, assuming that the dephasing probability $p(t)$ is simply given by $p = \frac{1}{2}(1 + e^{-\Gamma_\phi t})$.

More generally, the dephasing probability $p(t)$ maybe expressed as,

$$p(t) = \frac{1}{2}(1 + e^{-\chi(t)}). \quad (4)$$

In this case, the noisy density matrix in Eq. (A3) gets modified to Eq. (2). This elucidates the connection between the two different approaches by demonstrating how the decoherence functional can be utilized to derive the explicit probabilities within the Kraus operator framework.

This connection makes a more precise simulation of noisy dynamics possible, bridging the gap between theoretical descriptions and practical implementations of quantum systems under the influence of noise. Therefore, critical information on qubit dynamics can be derived from the noise spectral density, $S(\omega)$, which characterizes the environment. Extracting $S(\omega)$ from the measured signal, however, is not straightforward, as the process typically involves a deconvolution prone to error. Recent work [25] suggests that this problem can be

largely mitigated through the use of deep feedforward neural networks as explained in the subsequent section.

III. NOISE SPECTROSCOPY & MITIGATION METHODOLOGY

The proposed methodology is designed specifically to extract the noise spectrum $S(\omega)$ associated with T_ϕ relaxation noise. Experimentally, the T_ϕ decay function is isolated by removing the T_1 contribution from the overall T_2 decay. While T_1 relaxation can be addressed primarily through improved qubit fabrication and quantum error correction, our focus here is on estimating and mitigating dephasing noise.

The key element of our approach is a neural network trained to produce the noise spectrum $S(\omega)$ affecting a given qubit when it is provided with the coherence decay function $C(t)$ of that qubit as an input. We assume that $S(\omega)$ is stationary, Gaussian, and couples exclusively along the qubit's z -axis, which is a well-studied characteristic of dephasing noise. By leveraging the information from the noise spectrum, we then optimize the DD pulse sequence used to probe the T_2 decay. Our method is schematically shown in Fig. 1 and comprises the following steps:

1. *Training Data Generation*: Based on the previous work [30], we assumed that the noise spectra $S(\omega)$ follow some complex yet well-defined functional form. Particularly, we considered that white noise dominates at relatively low frequencies, $1/\omega$ -type noise becomes prominent at intermediate frequencies, and $k/(k^2 + \omega^2)$ -type noise takes over

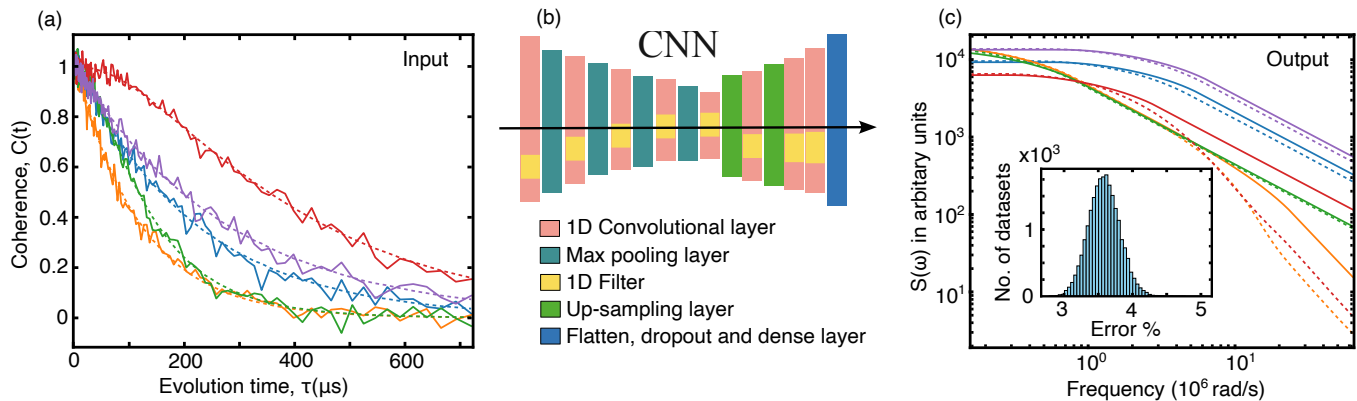


FIG. 1. (a) Randomly chosen 5 test input decoherence curves as functions of evolution time; the dashed lines denote the curves evaluated from the predicted $S(\omega)$. (b) A schematic diagram of the neural network developed in this work. (c) The numerically generated (solid lines) and the predicted (dashed line) noise spectra associated with the input decoherence curves. The inset shows a histogram of the estimation errors.

at relatively high frequencies. Thus, we generated tens of thousands of noise spectral densities $S(\omega)$ by varying noise amplitudes and frequency cutoffs associated with the aforementioned noise types. Additionally, the stitched noise spectra were smoothed to avoid unrealistic discontinuities. We then used Eq. (3) to evaluate the corresponding decoherence curves $C(t)$ by convoluting the generated noise spectra with the CPMG-32 filter function. Finally, we added random noise to the coherence curves $C(t)$ to simulate experimental noise. More details on data generation can be found in the Appendix B.

2. *Network Construction and Training:* Using the numerically generated noise spectral densities and their associated coherence curves $C(t)$, we trained a convolution neural network [25] to identify the noise spectral density $S(\omega)$ based on a single decoherence curve $C(t)$ provided at the network input. A detailed description is provided in Appendix B.
3. *Experimental Data Acquisition:* For experimental validation, we performed measurements on IBM’s superconducting quantum processors using the Qiskit package. After determining the optimal amplitude for the square-shaped π -pulse, we performed T_1 and T_2 decay experiments using a CPMG-32 pulse protocol. The choice of CPMG-32 sequence over conventional Hahn-echo protocol was made to enable probing of the complex high-frequency region of the noise spectrum, which lies beyond the white noise-dominated low-frequency region. Using the T_1 and T_2 data we generated the pure dephasing T_ϕ decay as per Eq. (5), where P_0 and P_1 are the probabilities of $|0\rangle$ (for T_2) and $|1\rangle$ (for T_1):

$$C(t) = e^{-\chi(t)} \sim \frac{e^{-\Gamma_2 t}}{\sqrt{e^{-\Gamma_1 t}}} = \frac{P_0(T_2)}{\sqrt{P_1(T_1)}} \quad (5)$$

4. *Noise Spectra Prediction:* The noise spectrum prediction is then obtained almost instantaneously, by providing the acquired experimental data as an input to our trained neural network.
5. *Optimization of DD Pulses:* The optimization begins by defining the filter function $F(\omega t)$ corresponding to a given DD sequence. By substituting the extracted noise spectrum $S(\omega)$ into Eq.(3), one can effectively obtain an objective function that seeks to minimize $\chi(t)$. The goal is to find the optimal timing of pulses that reduces the overlap between $S(\omega)$ and $F(\omega t)$. We obtained nearly optimal control pulse sequences by using the SciPy optimizer [35] – the Sequential Least Squares Programming (SLSQP) algorithm [36] to optimize the pulse sequence. Subsequently, the customized protocols were implemented on the investigated qubits to validate their fidelity.

IV. RESULTS AND DISCUSSION

A. Network Performance on the Test Data

We trained the neural network on a subset of the generated pairs of decoherence curves $C(t)$ and noise spectra $S(\omega)$ (the ‘training’ set). To then test the ability of the trained network to produce the correct noise spectrum from a single decoherence curve, we used another subset of the data (the ‘test’ set) and compared the noise spectrum produced by our network with the originally generated one. The solid lines in Fig. 1(c) represent the ‘test’ noise spectra, which were used to obtain the corresponding ‘test’ coherence curves, shown in solid lines in Fig. 1(a), by applying Eq. 3. The dashed lines in Fig. 1(c) are then the noise spectra obtained by applying the trained model to the ‘test’ coherence curves. The accuracy of the model prediction is excellent with a mean

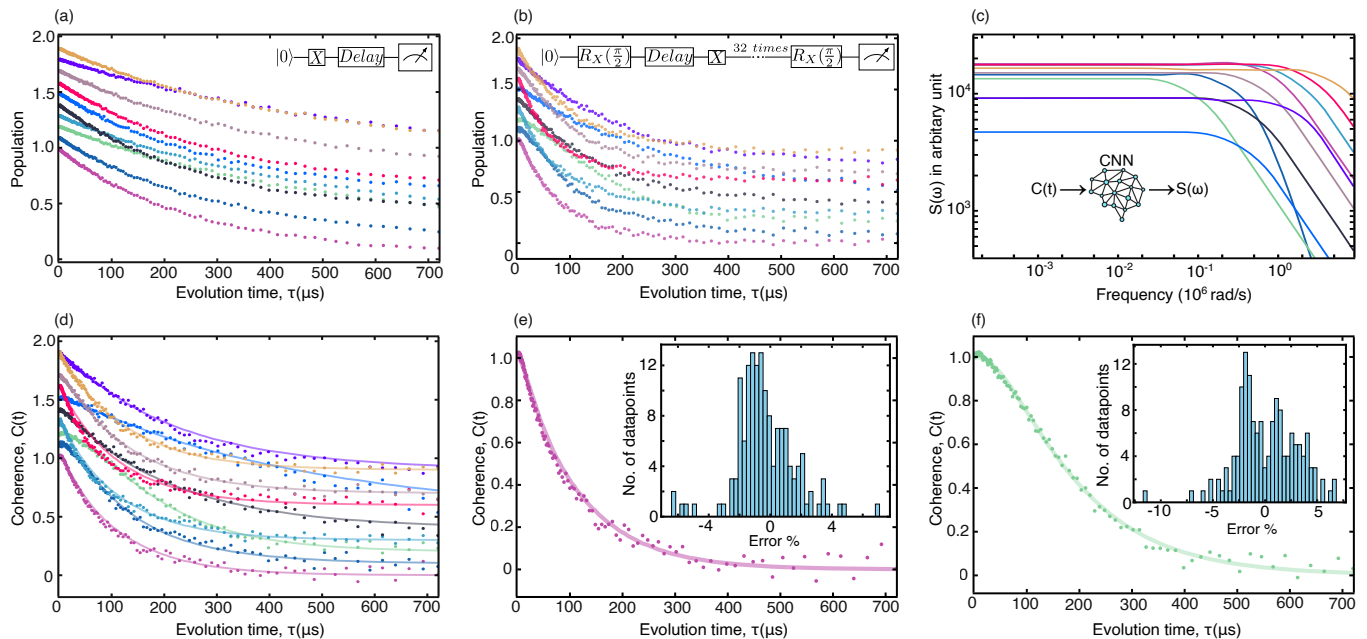


FIG. 2. (a), (b), and (d) display T_1 , T_2 and T_ϕ data respectively for 10 qubits on IBM Osaka. Each curve represents a qubit, with a vertical shift of 0.1 units for enhanced visibility. Dots indicate the experimental data, while in (d) the solid lines represent the network’s predictions. The extracted noise spectra are shown in subplot (c). For clarity, (e), and (f) show experimental and predicted decoherence curves for 2 qubits with the absolute error histogram in the inset.

absolute error of 3.6%, as shown in the inset. Note that this error is largely limited by the random noise added to the training data to mimic the experimental signal-to-noise ratio, suggesting that the performance of the network is near optimal. As a final check, the neural network-produced noise spectra were used to obtain decoherence curves to see how well those match the ‘test’ decoherence curves that had been given as an input to the network. These are plotted in dashed lines in Fig. 1(a), and indeed show good agreement with the ‘test’ decoherence curves, while demonstrating the de-noising capabilities of our network.

B. Network Performance on IBM Qubits

We tested our noise spectroscopy methodology on IBM’s superconducting qubits, specifically on the 127-qubit device, IBM Osaka. We specifically selected qubits with coherence times T_2 between 150 μs and 300 μs . The frequency range probed was determined by the total evolution time of the qubit—from 2 μs to 720 μs , which allowed sufficient coverage of both the low and the high-frequency regimes. A CPMG-32 pulse sequence was used with a π -pulse width of 48 ns. The results of T_1 and T_2 (CPMG-32) experiments shown in Fig. 2(a) and (b) illustrate the decay of the population of state $|0\rangle$ as a function of the evolution time τ . After processing the data as discussed in the previous section,

these curves were fed into a trained model to extract the noise spectra presented in Fig. 2(c). In Fig. 2(d) the dots represent experimental data, while the solid lines correspond to the curves estimated using the network’s predictions. The analysis revealed that the noise spectrum predominantly exhibited white noise characteristics, with a $1/\omega$ -type profile emerging around 1 MHz, confirming the model’s effectiveness in identifying dominant noise features. The model accurately predicted the noise spectrum for each qubit, as evidenced by a minimal prediction error in the coherence functions reconstructed from the extracted noise spectra; two example curves are shown in Fig. 2(e) and (f). The histograms of the error distribution are plotted in the insets of Fig. 2(e) and (f), indicated a symmetric distribution around zero, suggesting, yet again, that the errors were mostly limited by the experimental noise.

C. Optimization of Dynamical Decoupling Pulse Sequence

The predicted noise spectra were then used to develop the optimal sequences with varied number n of π -pulses. Based on the $1/\omega$ frequency cut-off in the noise spectra, we estimated that the $n = 8$ π -pulse sequences should provide the maximum advantage. Our experimental results, obtained on IBM Osaka quantum processor for two different qubits are displayed in Fig. 3(a) and (e) with

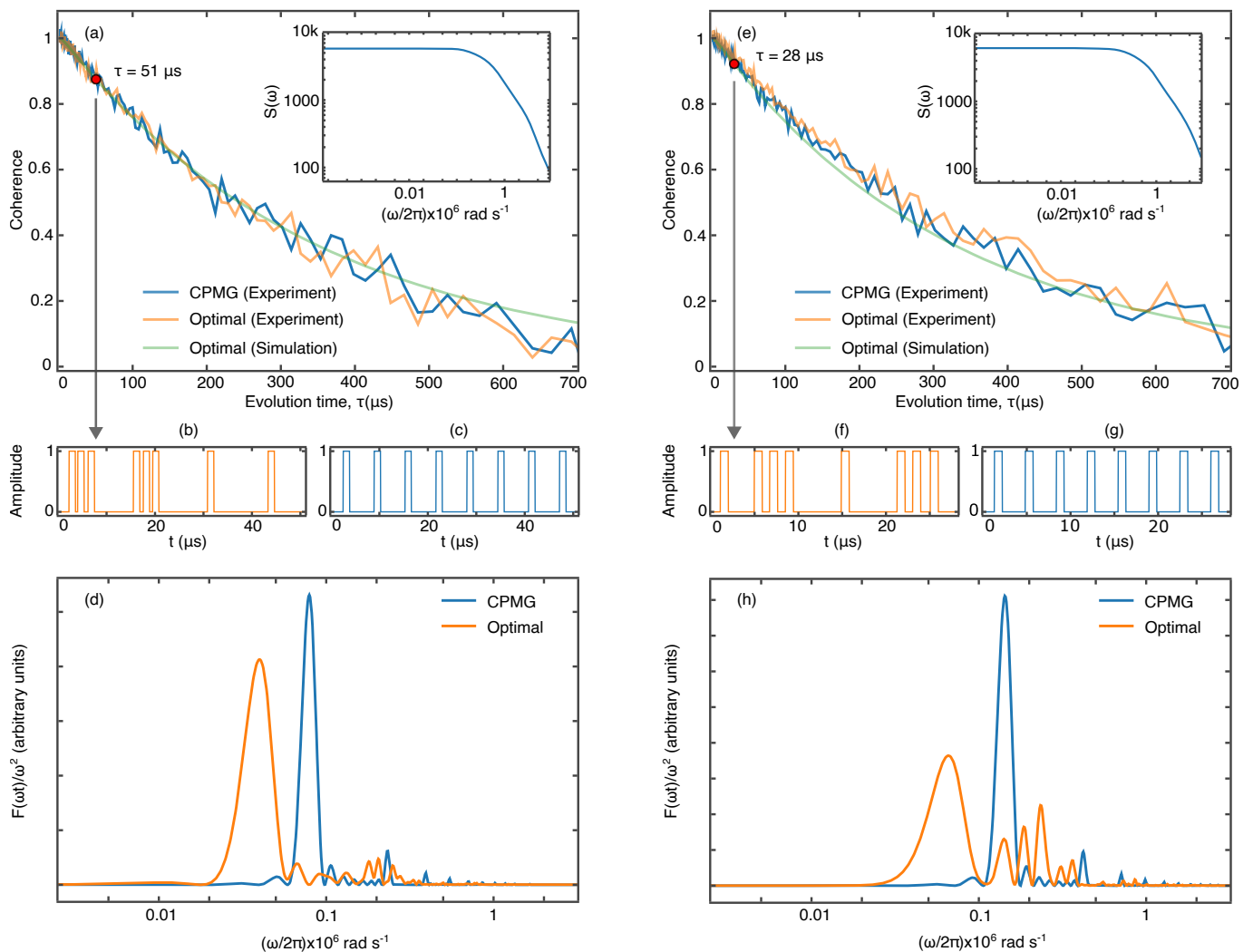


FIG. 3. The first and second columns correspond to two different qubits from IBM-Osaka. (a), (e) Decoherence curves $C(t)$ and noise spectra $S(\omega)$ associated with the given qubit. The coherence curve is obtained by applying CPMG-8 and optimal pulse sequences ($n = 8$). The blue and orange lines show the experimental coherence curves, while the green line shows the simulated optimal coherence curve. (b), (f) CPMG-8 and (c), (g) optimal pulse sequences for the given evolution time (pulse-widths are not to the scale). (d), (h) Filter functions $F(\omega t)$ corresponding the pulse sequences.

the underlying noise spectra plotted in the insets. The results reveal two notable outcomes. Firstly, the customized pulse sequences shown in Fig. 3(b) and (f) do not show noticeable improvement as compared to traditional protocols displayed in Fig. 3(c) and (g). This is due to the fact that the noise spectra are heavily white noise dominated and, consequently, the modified filter functions shown in Fig. 3(d) and (h) are unable to suppress the overlap. Secondly, despite implementing non-trivial bespoke pulse sequences, the experimental decoherence curves closely match with those predicted via the optimization algorithm. This authenticates the accuracy of the noise spectra predicted by the network. The overall methodology is, thus, a step forward in the noise-adapted optimal quantum error mitigation techniques. The effectiveness of the optimized sequences should certainly be

notable for other qubit systems where white noise is not the leading type of the environmental noise.

D. Rapid Time Dependent Noise Spectroscopy

In order to capture the time-evolution of the noise around IBM qubits, we performed time-dependent noise spectroscopy experiments on a qubit. To achieve this, ten T_1 , and ten T_2 measurements were performed consecutively while keeping the experimental parameters unchanged. Note that each run consists of 4000 shots to attain sufficient signal-to-noise ratio which required approximately 10 minutes to complete. The results displayed in Fig. 4(a) and (b) demonstrate that we are indeed able to record the rapid changes in T_1 and T_2

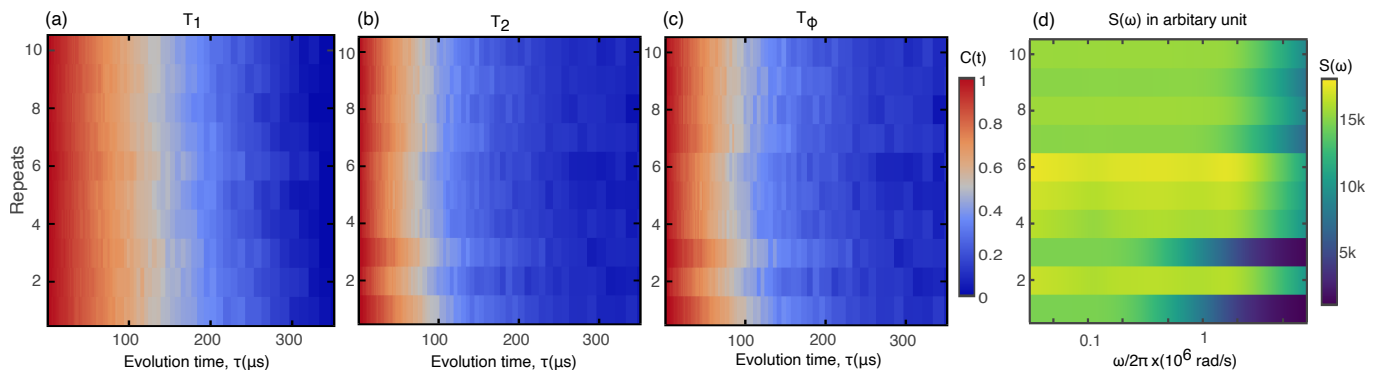


FIG. 4. (a)—(c) Heatmaps displaying time-dependent T_1 , T_2 , and T_ϕ datasets for 10 repeats on the same qubit. (d) Heatmap of the predicted noise-spectra associated with each repeat.

curves. Moreover, the extracted noise spectra presented in Fig.4(c) indicate that the discontinuous jumps in the dephasing and relaxation data are neither time-correlated nor entirely interdependent. These observations confirm that our noise spectroscopy model is a very effective tool to extract quasi-instantaneous noise profiles.

V. OUTLOOK

Owing to the universality of the technique discussed here, we anticipate this study will help examine and benchmark various quantum systems in the near future. We expect that the noise characterization methodology discussed here will provide useful insights to improve the engineering aspects of quantum systems. The fidelity of the current methodology can be improved by taking into account advanced gates [37], or DRAG pulses [38, 39], which are optimized to reduce leakage error, instead of square pulses. This should be possible owing to the recent advancements in the filter function formalism, which allows for analytical representation of arbitrary quantum control sequence [40–43]. Moreover, if this methodology is employed in conjunction with appropriate instrumentation such as Field Programmable Gate Arrays (FPGAs) [44], then instantaneous error mitigation strategies can potentially be developed.

It is important to reemphasize that the decoherence functional, $\chi(t)$, which depends on the knowledge of the environmental noise spectrum is intricately linked to the error rates of the various noise operators in the Kraus picture. Since Kraus formalism is commonly employed in the design and implementation of quantum error correction (QEC) protocols, having precise knowledge of the decoherence functional opens up new avenues for noise-adapted error correction protocols [45]. Indeed, QEC protocols can then be tailored to deal with a specific spectral range of noise. With the help of a trained model, time-dependent quantum error correction protocols can become a foreseeable reality.

VI. ACKNOWLEDGEMENTS

S.D. thanks the Indian Institute of Technology, Madras, India, for its seed and initiation grants. We acknowledge the use of facilities supported by a grant from the Mphasis F1 Foundation given to the Centre for Quantum Information, Communication, and Computing (CQuICC). Finally, we appreciate the use of IBM Quantum for this work. The views expressed are those of the authors and do not reflect the official policy or position of IBM or the IBM Quantum team.

-
- [1] W. H. Zurek, *Rev. Mod. Phys.* **75**, 715 (2003).
 - [2] M. Schlosshauer, *Rev. Mod. Phys.* **76**, 1267 (2005).
 - [3] G. Ithier, E. Collin, P. Joyez, P. Meeson, D. Vion, D. Esteve, F. Chiarello, A. Shnirman, Y. Makhlin, J. Schrieffer, *et al.*, *Physical Review B* **72**, 134519 (2005).
 - [4] H. Putterman, K. Noh, C. T. Hann, G. S. MacCabe, S. Aghaeimebodi, R. N. Patel, M. Lee, W. M. Jones, H. Moradinejad, R. Rodriguez, *et al.*, *arXiv preprint arXiv:2409.13025* (2024).
 - [5] A. M. Dalzell, S. McArdle, M. Berta, P. Bienias, C.-F. Chen, A. Gilyén, C. T. Hann, M. J. Kastoryano, E. T. Khabiboulline, A. Kubica, G. Salton, S. Wang, and F. G. S. L. Brandão, *arXiv preprint arXiv:2310.03011* (2023).
 - [6] F. Dolde, H. Fedder, M. W. Doherty, T. Nöbauer, F. Rempp, G. Balasubramanian, T. Wolf, F. Reinhard, L. C. L. Hollenberg, F. Jelezko, and J. Wrachtrup, *Nature Physics* **7**, 459 (2011).
 - [7] C. L. Degen, F. Reinhard, and P. Cappellaro, *Rev. Mod. Phys.* **89**, 035002 (2017).
 - [8] P. Szankowski, G. Ramon, J. Krzywda, D. Kwiatkowski, and L. Cywinski, *Journal of Physics: Condensed Matter* **29**, 333001 (2017).

- [9] L. Cywiński, R. M. Lutchyn, C. P. Nave, and S. Das Sarma, *Phys. Rev. B* **77**, 174509 (2008).
- [10] S. Hernández-Gómez, F. Poggiali, P. Cappellaro, and N. Fabbri, *Phys. Rev. B* **98**, 214307 (2018).
- [11] N. Bar-Gill, L. M. Pham, C. Belthangady, D. Le Sage, P. Cappellaro, J. R. Maze, M. D. Lukin, A. Yacoby, and R. Walsworth, *Nature Communications* **3**, 858 (2012).
- [12] J. Medford, L. Cywiński, C. BarCarrthel, C. M. Marcus, M. P. Hanson, and A. C. Gossard, *Phys. Rev. Lett.* **108**, 086802 (2012).
- [13] K. Khodjasteh and D. A. Lidar, *Phys. Rev. Lett.* **95**, 180501 (2005).
- [14] H. Y. Carr and E. M. Purcell, *Phys. Rev.* **94**, 630 (1954).
- [15] E. L. Hahn, *Phys. Rev.* **80**, 580 (1950).
- [16] G. S. Uhrig, *Phys. Rev. Lett.* **98**, 100504 (2007).
- [17] H. Uys, M. J. Biercuk, and J. J. Bollinger, *Phys. Rev. Lett.* **103**, 040501 (2009).
- [18] B. M. Terhal, Reviews of Modern Physics **87**, 307 (2015).
- [19] A. Jayashankar and P. Mandayam, Journal of the Indian Institute of Science **103**, 497 (2023).
- [20] K. S. Chou, T. Shemma, H. McCarrick, T.-C. Chien, J. D. Teoh, P. Winkel, A. Anderson, J. Chen, J. C. Curtis, S. J. de Graaf, J. W. O. Garmon, B. Gudlewski, W. D. Kalfus, T. Keen, N. Khedkar, C. U. Lei, G. Liu, P. Lu, Y. Lu, A. Maiti, L. Mastalli-Kelly, N. Mehta, S. O. Mundhada, A. Narla, T. Noh, T. Tsunoda, S. H. Xue, J. O. Yuan, L. Frunzio, J. Aumentado, S. Puri, S. M. Girvin, S. H. Moseley, and R. J. Schoelkopf, *Nature Physics* (2024), 10.1038/s41567-024-02539-4.
- [21] S. Heußen, D. F. Locher, and M. Müller, *PRX Quantum* **5**, 010333 (2024).
- [22] G. A. Álvarez and D. Suter, *Phys. Rev. Lett.* **107**, 230501 (2011).
- [23] L. M. Norris, D. Lucarelli, V. M. Frey, S. Mavadia, M. J. Biercuk, and L. Viola, *Phys. Rev. A* **98**, 032315 (2018).
- [24] D. F. Wise, J. J. Morton, and S. Dhomkar, *PRX Quantum* **2**, 010316 (2021).
- [25] F. Meneses, D. F. Wise, D. Pagliero, P. R. Zangara, S. Dhomkar, and C. A. Meriles, *Phys. Rev. Appl.* **18**, 024004 (2022).
- [26] M. Papić and I. de Vega, *Phys. Rev. A* **105**, 022605 (2022).
- [27] E. Canonici, S. Martina, R. Mengoni, D. Ottaviani, and F. Caruso, *Advanced Quantum Technologies* **7** (2023), 10.1002/qute.202300192.
- [28] Y. Lu, Z. Chen, Z. Ma, and S. Fei, *Advanced Quantum Technologies* (2025), 10.1002/qute.202400521.
- [29] J. Bylander, S. Gustavsson, F. Yan, F. Yoshihara, K. Harrabi, G. Fitch, D. G. Cory, Y. Nakamura, J.-S. Tsai, and W. D. Oliver, *Nature Physics* **7**, 565–570 (2011).
- [30] P. Krantz, M. Kjaergaard, F. Yan, T. P. Orlando, S. Gustavsson, and W. D. Oliver, *Applied Physics Reviews* **6** (2019), 10.1063/1.5089550.
- [31] H.-P. Breuer and F. Petruccione, *The theory of open quantum systems* (Oxford University Press, USA, 2002).
- [32] D. Manzano, *AIP Advances* **10** (2020), 10.1063/1.5115323.
- [33] D. Fernández de la Pradilla, E. Moreno, and J. Feist, *Phys. Rev. A* **109**, 062225 (2024).
- [34] M. A. Nielsen and I. L. Chuang, *Quantum Computation and Quantum Information: 10th Anniversary Edition* (Cambridge University Press, 2011).
- [35] P. Virtanen, R. Gommers, T. E. Oliphant, M. Haberland, T. Reddy, D. Cournapeau, E. Burovski, P. Peterson, W. Weckesser, J. Bright, S. J. van der Walt, M. Brett, J. Wilson, K. J. Millman, N. Mayorov, A. R. J. Nelson, E. Jones, R. Kern, E. Larson, C. J. Carey, Í. Polat, Y. Feng, E. W. Moore, J. VanderPlas, D. Laxalde, J. Perktold, R. Cimrman, I. Henriksen, E. A. Quintero, C. R. Harris, A. M. Archibald, A. H. Ribeiro, F. Pedregosa, P. van Mulbregt, and SciPy 1.0 Contributors, *Nature Methods* **17**, 261 (2020).
- [36] D. Kraft, *A Software Package for Sequential Quadratic Programming*, Deutsche Forschungs- und Versuchsanstalt für Luft- und Raumfahrt Köln: Forschungsbericht (Wiss. Berichtswesen d. DFVLR, 1988).
- [37] Y. Baum, M. Amico, S. Howell, M. Hush, M. Liuzzi, P. Mundada, T. Merkh, A. R. Carvalho, and M. J. Biercuk, *PRX Quantum* **2**, 040324 (2021).
- [38] M. Werninghaus, D. J. Egger, F. Roy, S. Machnes, F. K. Wilhelm, and S. Filipp, *npj Quantum Information* **7**, 14 (2021).
- [39] E. Hyyppä, A. Vepsäläinen, M. Papić, C. F. Chan, S. Inel, A. Landra, W. Liu, J. Luus, F. Marxer, C. Ockeloen-Korppi, S. Orbell, B. Tarasinski, and J. Heinsoo, *arXiv preprint arXiv:2402.17757* (2024).
- [40] A. Soare, H. Ball, D. Hayes, J. Sastrawan, M. C. Jarratt, J. J. McLoughlin, X. Zhen, T. J. Green, and M. J. Biercuk, *Nature Physics* **10**, 825 (2014).
- [41] P. Cerfontaine, T. Hangleiter, and H. Bluhm, *Phys. Rev. Lett.* **127**, 170403 (2021).
- [42] T. Chalermputitarak, B. Tonekaboni, Y. Wang, L. M. Norris, L. Viola, and G. A. Paz-Silva, *PRX Quantum* **2**, 030315 (2021).
- [43] I. N. M. Le, J. D. Teske, T. Hangleiter, P. Cerfontaine, and H. Bluhm, *Phys. Rev. Appl.* **17**, 024006 (2022).
- [44] U. Goldblatt, N. Kahn, S. Hazanov, O. Milul, B. Guttel, L. M. Joshi, D. Chausovsky, F. Lafont, and S. Rosenblum, *Phys. Rev. X* **14**, 041056 (2024).
- [45] D. Biswas, G. M. Vaidya, and P. Mandayam, *Phys. Rev. Res.* **6**, 043034 (2024).

Appendix A: Noise Model: Kraus Operator Picture

Kraus formalism provides a comprehensive framework for modeling noise by representing the system’s evolution through a set of operators, known as Kraus operators, that describe the impact of noise on the quantum system. This formalism allows for a clear and systematic analysis of various types of noise processes, including decoherence and dissipation, by translating them into a mathematical language that is both intuitive and versatile.

The evolution of a quantum system, such as a qubit, can be known mathematically via *completely positive trace preserving* (CPTP) maps. If the decoherence interactions is known, we can analytically write a map which gives us the final density matrix of our system [34]. Let $\rho_S \otimes \Phi_E$ be the initial unentangled state of the system and environment, and let U_{SE} denote the unitary time-evolution operator that arises due to system—environment interaction. Then, the final state of the sys-

tem alone can be obtained as follows:

$$\mathcal{E}(\rho_S) = \text{Tr}_E[U_{SE}(\rho_S \otimes \Phi_E)U_{SE}^\dagger] \quad (\text{A1})$$

where the physical process map \mathcal{E} on the system operator Hilbert space \mathcal{H}_S must be completely positive (CP). The complete positivity of the map implies the existence of an operator—sum decomposition for the map [34], of the following form

$$\mathcal{E}(\rho) = \sum_{i=1}^N E_i \rho E_i^\dagger \quad (\text{A2})$$

This is known as Choi–Kraus–Sudarshan operator–sum representation, where $\{E_i\}$ are a set of operators known as Kraus operators on the state space of the system. The operators satisfy a completeness relation that arises from the requirement that the trace of $\mathcal{E}(\rho)$ be equal to one. Such maps are said to be trace preserving (TP): $\text{Tr}[\mathcal{E}(\rho)] = 1 \implies \sum_i E_i^\dagger E_i = I_s$. Knowing the map \mathcal{E} is equivalent to knowing the Kraus operators $\{E_i\}_{i=1}^N$. Here, N depends on the number of basis states used to define the environment.

We will now describe two examples of such CPTP maps – also referred to as *quantum channels* [34]— which become important in the context of superconducting qubits. The first is the so called *amplitude damping* channel, which characterizes the effects due to loss of energy from a quantum system. Specifically, it describes energy dissipation in a two-level system. Let $|0\rangle$ denote the ground state and $|1\rangle$ some excited state of a qubit. Then, the amplitude damping channel denoted as $\mathcal{E}^{AD} = \{E_0^{AD}, E_1^{AD}\}$, is described by the following pair of Kraus operators [34].

$$\begin{aligned} E_0^{AD} &= \frac{1}{2}[(1 + \sqrt{1-\gamma})I + (1 - \sqrt{1-\gamma})\sigma_z] \\ &= \begin{pmatrix} 1 & 0 \\ 0 & \sqrt{1-\gamma} \end{pmatrix} \\ E_1^{AD} &= \frac{\sqrt{\gamma}}{2}[\sigma_x + i\sigma_y] = \begin{pmatrix} 0 & \sqrt{\gamma} \\ 0 & 0 \end{pmatrix} \end{aligned}$$

Here, $\{I, \sigma_x, \sigma_y, \sigma_z\}$ is the Pauli basis and γ is the probability of a transition from the excited state to the ground state. As a function of time, this transition probability can be expressed as $\gamma = 1 - e^{-\Gamma_1 t}$, where $\Gamma_1 = 1/T_1$ is the inverse of the relaxation time T_1 .

Another example of a noise process is that of *phase damping* channel, which describes the loss of relative phase information between the energy eigenstates. Then phase damping channel denoted as $\mathcal{E}^{PD} = \{E_0^{PD}, E_1^{PD}\}$, is described by the following pair of Kraus operators [34] given by

$$\begin{aligned} E_0^{PD} &= \sqrt{p}I = \begin{pmatrix} \sqrt{p} & 0 \\ 0 & \sqrt{p} \end{pmatrix} \\ E_1^{PD} &= \sqrt{1-p}\sigma_z = \begin{pmatrix} \sqrt{1-p} & 0 \\ 0 & -\sqrt{1-p} \end{pmatrix} \end{aligned}$$

Note that phase damping is also often referred to as the *phase flip* channel [34]. Here, p is the probability of not a phase flip. As a function of time, this probability can be expressed as, $p = \frac{1}{2}(1 + e^{-\Gamma_\phi t})$, where $\Gamma_\phi = 1/T_\phi$ is the inverse of the relaxation time T_ϕ .

Consider an arbitrary single-qubit state, written in the standard basis as, $|\psi\rangle = \alpha|0\rangle + \beta|1\rangle$. Let $\rho = |\psi\rangle\langle\psi|$ denote the density operator corresponding to this state. Then, the density operator after the combined action of both these noise processes is given by

$$\begin{aligned} \rho &= \begin{pmatrix} |\alpha|^2 & \alpha\beta^* \\ \alpha^*\beta & |\beta|^2 \end{pmatrix} \xrightarrow{\text{noise}} \rho_{\text{noisy}} = \mathcal{E}^{AD} \circ \mathcal{E}^{PD}(\rho) \\ &= \begin{pmatrix} 1 + (|\alpha|^2 - 1)e^{-\Gamma_1 t} & \alpha\beta^* e^{-\frac{\Gamma_1}{2}t} e^{-\Gamma_\phi t} \\ \alpha^*\beta e^{-\frac{\Gamma_1}{2}t} e^{-\Gamma_\phi t} & |\beta|^2 e^{-\Gamma_1 t} \end{pmatrix} \quad (\text{A3}) \end{aligned}$$

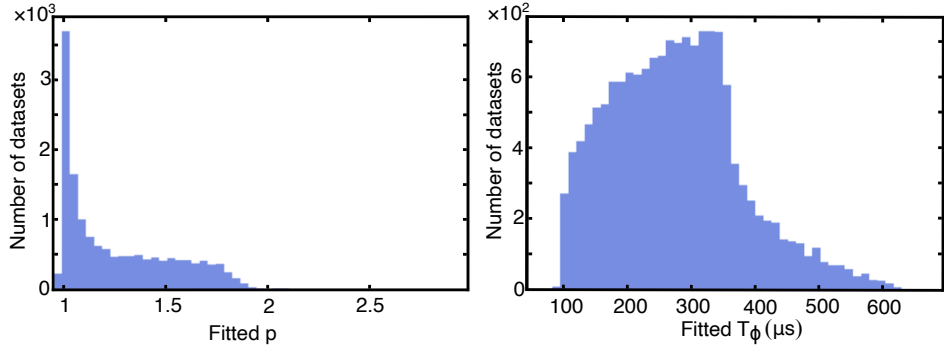
It does not matter in which order the noise acts since both noise processes are independent. In superconducting qubits, the dominant noises are amplitude damping, also referred to as energy relaxation or longitudinal relaxation, and phase damping, also referred to as pure dephasing.

Appendix B: Neural Network

We used TensorFlow Keras Python module to train our convolutional neural network and to perform the noise spectra predictions from the experimentally obtained decoherence curves. The autoencoder-type network, as described in Table II alternates between convolutional and pooling operations to progressively extract features from the input data, and the upsampling restores the data's original dimensions while enhancing feature representation. The final dense layer aims to produce a linear output appropriate for regression or other continuous output tasks. Our network is trained for approximately 75 epochs, achieving an accuracy loss lower than 4%. The training and validation losses, measured as mean absolute error, are monitored over epochs. Furthermore, to obtain a high degree of prediction accuracy, it is essential to constrain the training data appropriately. We fit the generated decoherence curves using a stretched exponential function:

$$\tilde{C}(t) = e^{-(t/T_\phi)^p} \quad (\text{B1})$$

Although, the simulated curves cannot be exactly fitted with Eq.B1, this method provides a good measure to filter the training data. Fig 5 shows the final distribution of the stretching factor p , and of inverse decay rate T_ϕ in the training dataset. All the experimental curves lie well within the chosen bounds.

FIG. 5. Distribution of fitted p and T_ϕ in the training dataset

Layer (Type)	Output Shape	Parameters	Activation	Notes
Input Layer	(xtrain size, 1)	0	-	Accepts one-dimensional data
Conv2D (1)	(None, xtrain size, 40)	1040	ReLU	40 filters, 5x5 kernel, same padding
MaxPooling2D (1)	(None, xtrain size, 40)	0	-	Pool size = 'pool size', same padding
Conv2D (2)	(None, xtrain size, 40)	40040	ReLU	40 filters, 5x5 kernel, same padding
MaxPooling2D (2)	(None, xtrain size, 40)	0	-	Pool size = 'pool size', same padding
Conv2D (3)	(None, xtrain size, 40)	40040	ReLU	40 filters, 5x5 kernel, same padding
MaxPooling2D (3)	(None, xtrain size, 40)	0	-	Pool size = 'pool size', same padding
Conv2D (4)	(None, xtrain size, 40)	40040	ReLU	40 filters, 5x5 kernel, same padding
MaxPooling2D (4)	(None, xtrain size, 40)	0	-	Pool size = 'pool size', same padding
Conv2D (5)	(None, xtrain size, 80)	80080	ReLU	80 filters, 5x5 kernel
UpSampling2D (1)	(None, xtrain size, 80)	0	-	Upsampling size = 'pool size'
Conv2D (6)	(None, xtrain size, 160)	160160	ReLU	160 filters, 5x5 kernel
UpSampling2D (2)	(None, xtrain size, 160)	0	-	Upsampling size = 'pool size'
Conv2D (7)	(None, xtrain size, 320)	320320	ReLU	320 filters, 5x5 kernel
Conv2D (8)	(None, xtrain size, 1)	8001	ReLU	1 filter, 5x5 kernel
Flatten	(None, xtrain size)	0	-	Converts to 1D vector
Dropout	(None, xtrain size)	0	-	Dropout rate = 'dropout rate'
Dense (1)	(None, 501)	xtrain size * 501 + 501	Linear	Final output layer
Total Parameters: 769,721				

TABLE II. Summary of the Network. Here typical xtrain size = 150, 'pool size' = 2, and 'dropout rate' = 0.05.